

An Amorphous Peri-Implant Ligament with Combined Osteointegration and Energy-Dissipation

Junyu Hou, Zuohui Xiao, Zengqian Liu, Hwei Zhao, Yankun Zhu, Lin Guo,*
Zhefeng Zhang, Robert O. Ritchie,* Yan Wei,* and Xuliang Deng*

Progress toward developing metal implants as permanent hard-tissue substitutes requires both osteointegration to achieve load-bearing support, and energy-dissipation to prevent overload-induced bone resorption. However, in existing implants these two properties can only be achieved separately. Optimized by natural evolution, tooth-periodontal-ligaments with fiber-bundle structures can efficiently orchestrate load-bearing and energy dissipation, which make tooth–bone complexes survive extremely high occlusion loads (>300 N) for prolonged lifetimes. Here, a bioinspired peri-implant ligament with simultaneously enhanced osteointegration and energy-dissipation is presented, which is based on the periodontium-mimetic architecture of a polymer-infiltrated, amorphous, titania nanotube array. The artificial ligament not only provides exceptional osteoinductivity owing to its nanotopography and beneficial ingredients, but also produces periodontium-similar energy dissipation due to the complexity of the force transmission modes and interface sliding. The ligament increases bone–implant contact by more than 18% and simultaneously reduces the effective stress transfer from implant to peri-implant bone by $\approx 30\%$ as compared to titanium implants, which as far as is known has not previously been achieved. It is anticipated that the concept of an artificial ligament will open new possibilities for developing high-performance implanted materials with increased lifespans.

of an implant is osteointegration, which achieves anchorage from surrounding bone to support daily load-bearing applications.^[2] Nevertheless, the established osteointegration could be significantly destroyed by overloads during long-term performance, accounting for the major risk of later implant failure.^[3,4] Therefore, designing an energy-dissipative implant to eliminate overload damage represents a promising strategy to prevent bone resorption and enhance clinical success. However, existing implants can only realize osteointegration or energy-dissipation separately.

To promote osteointegration, the previous literature has invariably focused on surface modification of the implant by controlling the geometry and topography, or by employing chemical agents.^[5–8] Nevertheless, the extremely high surface stiffness maintained by an implant can result in exceptionally low energy dissipation. To reduce overload damage, material engineering approaches have attempted to enhance energy dissipation by coating the implants with a soft polymer or polymer/ceramic composite.^[9–11] However, poor osseointegration and a low interfacial binding force can adversely affect the implant's longevity. Therefore, the fabrication of osteointegratable and energy-dissipative implants has become a major goal in materials science in order to significantly prolong their physiological lifespan.

1. Introduction

Metal implants with outstanding mechanical strength and fatigue resistance are the main choice of hard-tissue substitutes to reproduce physiological function.^[1] The primary requirement

J. Hou, H. Zhao, L. Guo
Beijing Advanced Innovation Center for Biomedical Engineering
School of Chemistry
Beihang University
Beijing 100191, P. R. China
E-mail: guolin@buaa.edu.cn

Z. Xiao, Y. Wei, X. Deng
Department of Geriatric Dentistry
NMPA Key Laboratory for Dental Materials
National Engineering Laboratory for Digital and Material
Technology of Stomatology
Beijing Laboratory of Biomedical Materials
Peking University School and Hospital of Stomatology
Beijing 100081, P. R. China
E-mail: kqweiyang@bjmu.edu.cn; kqdengxuliang@bjmu.edu.cn

 The ORCID identification number(s) for the author(s) of this article can be found under <https://doi.org/10.1002/adma.202103727>.

Z. Liu, Y. Zhu, Z. Zhang
Institute of Metal Research
Chinese Academy of Sciences
Shenyang 110016, P. R. China
R. O. Ritchie
Department of Materials Science and Engineering
University of California Berkeley
Berkeley, CA 94720, USA
E-mail: roritichie@lbl.gov

DOI: 10.1002/adma.202103727

In nature, the biological system of the tooth–bone complex can survive extremely high occlusion loads (>300 N).^[12] The exceptional capabilities for load-bearing and energy dissipation of this system originate from the hierarchical architecture of the periodontal ligaments (PDLs) at the interface between the tooth and bone. In PDLs, the oblique or perpendicular orientation of the collagen fiber bundles with respect to the tooth-root surface not only acts to anchor the tooth to the surrounding jawbone, but also forms an elastic cushion at the interface to provide flexibility.^[13] In such a manner, these unique structures can support normal mastication loads yet diminish the effects of occasional overloads.^[14] This principle provides a conceptual basis for coordinating osteointegration and energy-dissipation by fabricating ligament-like structures around metal implants. Recent exploration has tried to build ligament-like connective tissues at implant–bone interfaces by gradual optimized seeding of PDL cells or cell-sheets in endosseous or endodontic models.^[10,15] Although excellent energy dissipation can be achieved by these biological regenerations, their low stiffness cannot guide osteointegration to provide sufficient support for mastication load-bearing. To date, the rational design of PDL-like peri-implant ligaments (PIL) that can simultaneously fulfill the requirements for sufficient load-bearing and adequate energy dissipation has remained a challenge.

Here, inspired by the periodontium, we created an osteointegratable and energy-dissipative PIL composed of polymer-infiltrated amorphous arrays of titania nanotubes as energy-dissipative and osteoinductive units. The artificial ligament displays a periodontal-ligament-like hierarchical architecture, superior energy dissipation, and excellent inductivity on expression of osteogenic specific esterase, genes, and proteins. The resulting PIL simultaneously increases bone–implant contact by more than 18% and reduces the effective stress transfer from implant to the peri-implant bone by ≈30%.

2. Results and Discussion

Figure 1a shows that the PIL is deliberately constructed around a titanium (Ti) implant by starting with the in situ anodized growth of honeycomb-like titania nanotube arrays, followed by additional anodized formation of a compact oxide-interlayer and infiltration with cross-linked chitosan (CS). Scanning electron microscope (SEM) images show that the resultant PIL has a hierarchical architecture distinctly resembling that of a naturally occurring PDL (**Figure 1b**). The 3D profile, magnified detail, and cross-section views in a finite element modeling (FEM) simulation show that the PIL reduced the effective stress transfer from implant to peri-implant bone by a maximum of 30% compared to that of traditional Ti implants (**Figure 1b**). This result is derived from the periodontium-mimetic energy-dissipative effect of the polymer-infiltrated amorphous titania-nanotube-array units in the PIL. The nanotube-array parameters were optimized through experimental screening which determined that a height of ≈9 μm and an inner diameter of ≈80 nm had the highest mechanical performance (**Figure S1**, Supporting Information). The amorphous phase of the titania nanotubes (A-TNTs) was formed by a fast-chemical interaction between the titanium ions Ti^{4+} and oxygen ions O^{2-} in the electrolyte.^[16]

The electrolyte was 0.57 wt% ammonium fluoride in a mixed solvent of ethylene glycol and hydrogen peroxide (25:1, v:v). The homogeneous A-TNT structure with no obvious defects can be seen in the transmission electron microscopy (TEM) image of an individual nanotube wall in **Figure 1c**. The amorphous features of the titania nanotubes are demonstrated by Raman characterization, X-ray diffraction (XRD), high-resolution TEM (HRTEM), and the corresponding selected-area electron diffraction (SAED) pattern, all shown in **Figure S2a,b**, Supporting Information and **Figure 1d**. Moreover, the homogeneity of the A-TNT is evident from the uniform dispersion of the Ti and O elements, detected by Cs-corrected scanning transmission electron microscopy (STEM) imaging, and relevant electron energy loss spectroscopy (EELS) characterization, as shown in **Figure S2c–f**, Supporting Information.

To improve the interfacial adhesion between the A-TNT arrays and crystalline Ti substrate, we developed a facile method of additional anodization,^[17] as described in the Experimental Section. Using this method, a compact oxide layer, with a thickness of ≈170 nm, was created between the A-TNTs and Ti substrate, as shown in **Figure S3a,b**, Supporting Information. Uniaxial tensile testing along the axial direction of the A-TNTs indicated an approximately threefold increase in the interfacial adhesion strength as compared to those without the compact oxide layer. The A-TNTs with a compact layer possessed a markedly higher adhesion strength (≈9 MPa) than the A-TNTs without the layer (≈3 MPa) (**Figure S3c,d**, Supporting Information). The interfacial adhesion was further examined by immersing samples in phosphate buffer solution (PBS) with lysosome to simulate physiological conditions for different time-periods (1, 3, and 6 months; **Figure S3e**, Supporting Information). After treatment for 6 months, the adhesion strength only showed a small decrease to ≈8 MPa, indicative of a stable and strong interfacial connection. Furthermore, the weight degradation test showed that there was no significant mass reduction after in vitro degradation for 3 months, which illustrated the superior stability of the PIL (**Figure S4**, Supporting Information).^[18]

To simulate the role of glycosaminoglycans in natural ligaments as load dissipaters and lubricators,^[19,20] we infiltrated viscoelastic polymer into the A-TNTs by a vacuum-assisted process.^[21] This method helped to supplant all the air and promote the gradual filling of the inner cavities of the nanotubes and the interspaces between them. Moreover, the low cross-linked density (**Figure S5**, Supporting Information), as well as the high fluidity of the liquid-state chitosan, facilitated a seamless infiltration into the space within the nanotube arrays. After the polymer infiltration, the composite was left to dry at 20 °C. This generated a highly compliant network, which intertwined with the preferentially aligned nanotubes. Compared to chitosan, the cross-linked chitosan showed better stability,^[13] higher stiffness (Young's modulus of 4.98 ± 0.37 GPa), and higher energy dissipation efficiency (average loss factor of 0.054 ± 0.004 , from 10–100 Hz) (**Figure S6**, Supporting Information). The side (**Figure 1e,f** and **Figure S7**, Supporting Information) and top (**Figure S8a,b**, Supporting Information) views taken in the SEM show that the A-TNTs were filled with cross-linked chitosan to form an inorganic–organic nanocomposite overlayer on the Ti implant (**Figure S8c**, Supporting Information).

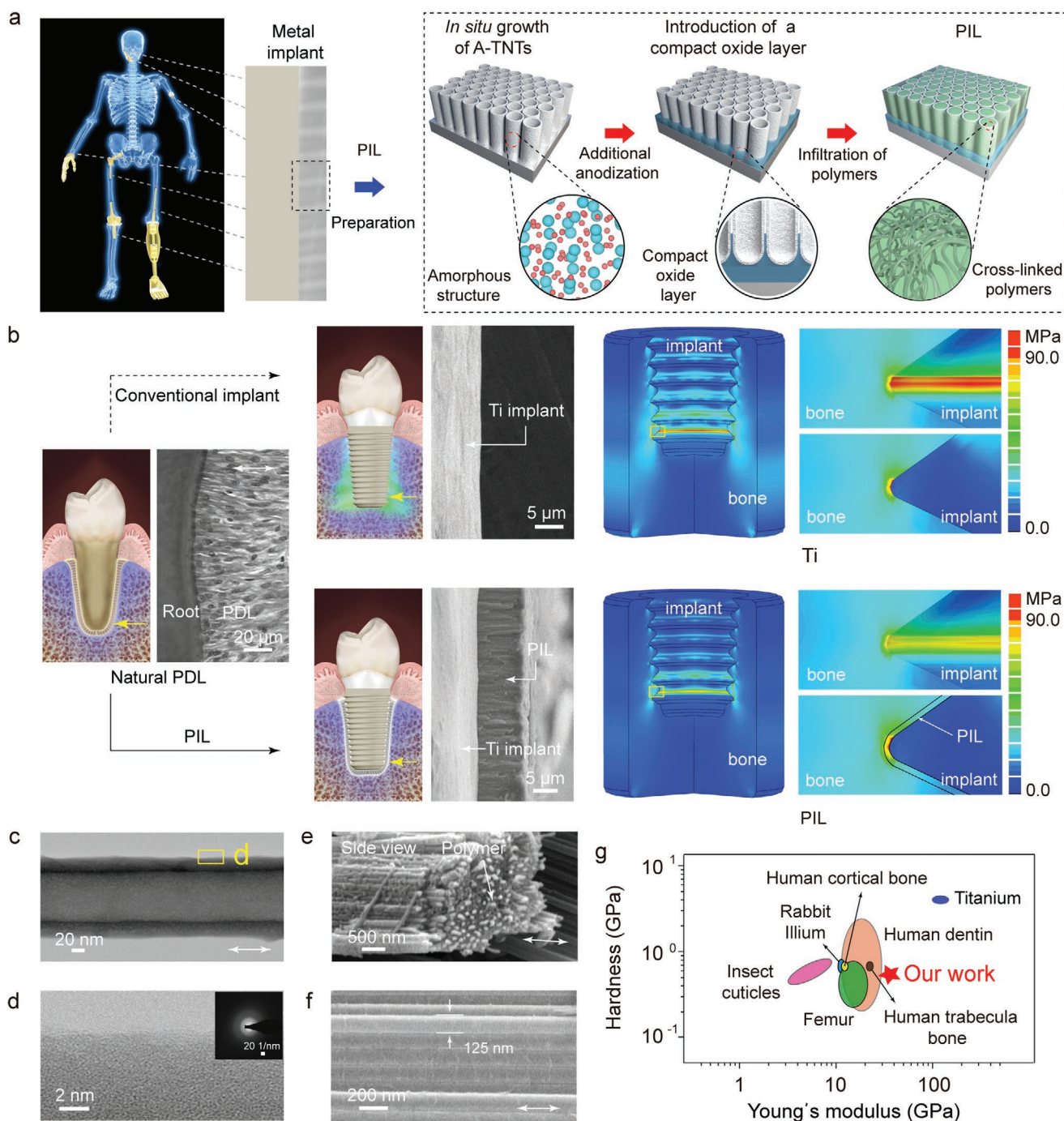


Figure 1. Synthesis approach, microstructure, and mechanical properties of the PIL. a) Schematic illustration of the synthetic PIL. Metal implants are now clinically applied as multiple hard-tissue substitutes such as synthetic tooth, hand, arm, leg, foot, and hip, all of which require ligaments to obtain excellent osteointegration and energy-dissipation. The synthetic PIL here was manufactured using a three-step procedure: *in situ* growth of the honeycomb-like A-TNT arrays, enhancing the adhesion of A-TNT arrays to the Ti substrate, and infiltration of the high damping polymer matrix. b) Due to the unique structure primarily composed of oriented collagen fiber bundles in natural PDL, the excessive forces over the alveolar bone could be reduced and redistributed. However, because of the lack of energy dissipation mechanisms, when force impacts the titanium implant, the alveolar bone receives a relatively high amount of mechanical stimulus. Due to the structural and functional similarity to natural counterparts, our modification of the implant in the PIL allows for increased energy absorption, which lessens the mechanical stress transmitted to the alveolar bone. More significant stress shielding of the alveolar bone can occur with the high elastic modulus of the titanium implants compared to the PIL, determined from finite element simulations. c) TEM image of an individual A-TNT. d) HRTEM image from the yellow frame of the A-TNT wall and the corresponding SAED pattern (inset), showing the halo ring feature of an amorphous structure. e, f) SEM images of the PIL showing the corresponding enlarged side view images. g) Comparison of mechanical properties, hardness vs stiffness, of the PIL with its competitor devices.

We next examined the micromechanical properties of the PIL. Figure S9a,b, Supporting Information show that the Young's modulus (E_Y) and hardness (H) achieved by the PIL were 27.6 ± 3.0 and 0.52 ± 0.03 GPa, respectively. 3D contour maps enable direct visualization of the local E_Y (average value of 27.3 ± 2.7 GPa) and H (average value of 0.51 ± 0.05 GPa), which display the homogeneity of nanomechanical properties in the PIL (Figure S9c,d, Supporting Information). These results suggest that the PIL provides a much closer mechanical performance to human bone as compared to the PIL-free titanium implant (Figure 1g and Table S1, Supporting Information).

With respect to the viscoelastic properties, these can be evaluated by the viscoelastic figure of merit for materials (VFOM) which is the product of the storage modulus and loss factor. The VFOM values for the PIL were in the range of 0.67 to 1.55 GPa, from 1–200 Hz, which is well above the presumed upper limit of 0.6 GPa for most traditional solid materials (Figure S10a and Table S2, Supporting Information).^[22,23] The weight adjusted VFOM for the PIL is typically higher than $0.8 \times 10^6 \text{ m}^2 \text{ s}^{-2}$, which also exceeds the benchmark for conventional structural materials.^[24] This results from the fact that our PIL displays a lower material density (ρ) than many other natural or synthetic viscoelastic materials (Figure S10b, Supporting Information). Moreover, a mechanical stability test using long-cycle compressions at a high load of 20 mN exhibited no significant decrease in PIL stiffness; indeed, 60% of the original modulus after 400 cycles was retained (Figure S11, Supporting Information). These results demonstrate that the PIL possesses an excellent mechanical stability and structural damage-resistance capacity. It has been well established that the bone-comparable stiffness could help prevent stress shielding effect,^[25] whereas materials with high VFOM and fatigue resistance are favorable for resisting long-term low-impact loads and increasing resilience to aging,^[24] which are critically important for the long-time service of the PIL. Thus, these mechanical properties provide a promising potential for the PIL to sustain the primary load-bearing function of implants.

To further explore the mechanism by which the PIL simulates the stress-tolerance effects of natural PDL, we examined the energy dissipation properties of the PIL subjected to quasi-static and dynamic loads by imitating three typical physiological occlusion situations, specifically: I) biting into food, II) continuous chewing motion, and III) instantaneous occlusion (Figure 2a). When imitating the load-bearing effects of “biting into food,” nano-indentation testing with a high load (20 mN) demonstrated that plastic deformation occurs at the exterior surface of the PIL with no visible microscopic crack or crack propagation (Figure S12, Supporting Information). Thereafter, we quantitatively evaluated the energy dissipation capability of the Ti substrate with and without the PDL using the energy dissipation index. The index represented the contribution of dissipated energy (W_d) by plastic deformation relative to the total energy ($W_t = W_d + W_e$),^[26] where W_e is the elastically stored energy. We found statistically significant differences in W_t between the Ti implant (4,193 nJ) and the PIL (12, 625 nJ). Moreover, $87.9 \pm 2.6\%$ of the total energy was dissipated in the PIL by plastic deformation, which is markedly higher than that in the Ti substrate ($76.4 \pm 2.3\%$; this is shown in Figure 2b and Figure S13, Supporting Information). This indicates that

the PIL can absorb a larger amount of mechanical energy than the PIL-free implant, thereby exhibiting significant mechanical function similar to natural PDLs.

To simulate the loading for “continuous chewing motion,” dynamic mechanical analysis (DMA) was performed to explore the energy dissipation characteristics under successive mechanical loads. Using the tangent of the phase angle, termed the loss factor $\tan\delta$, as a measurement of the damping capacity of materials,^[27] we found that the measured average loss factor of the PIL ($\tan\delta \approx 0.053 \pm 0.008$) was approximately five times higher than that of the non-modified Ti substrate (0.009 ± 0.0010) at a variety of frequencies (Figure 2c). The value of $\tan\delta$ also approached that of natural PDL over a wide range of frequencies (e.g., the $\tan\delta$ of human PDL is $\approx 0.078\text{--}0.13$ at 0.5–10 Hz,^[28] and bovine PDL is $\approx 0.04\text{--}0.08$ at 0.01–100 Hz).^[14] Further, the average $\tan\delta$ value of amorphous titania (0.012 ± 0.002) substantially exceeded that of crystalline titania (0.004 ± 0.002) at 1–100 Hz (Figure S14a, Supporting Information). Compared to bulk amorphous titania where $\tan\delta \approx 0.012 \pm 0.002$ (Figure S14b, Supporting Information), a significant increase in loss factor was measured for the A-TNT arrays ($\tan\delta \approx 0.021 \pm 0.007$). These results indicate that the amorphous design and the nanotube-array significantly enhance the dynamic energy dissipation of the PIL.

To simulate the loading with “instantaneous occlusion,” systematic finite element modeling was employed. The stress wave attenuation in the PIL at the nanoscale was examined as a function of propagation time. The FEM simulation shows that the PIL effectively attenuates the stress wave under dynamic loads (Figure 2e and Figure S15a, Supporting Information), imitating the elastic wave decay in a natural PDL. By comparison, the non-modified titanium implant exhibits a weak dissipation of the dynamic energy owing to its higher stiffness and lower damping capacity (Figure 2d), which also tends to cause bone loss in clinical applications (Figure 2f bottom and Figure S15b,c, Supporting Information).

Overall, these results indicate that the PIL possesses PDL-like energy dissipation properties, which are favorable for reducing and redistributing excessive stress to protect the bony anchorage. This can be attributed to the complexity of force transmission modes (Figure 2f top) and interface-sliding (Figure 2h) effects of the PIL. Due to the feature of long-range disorder,^[29–32] the amorphous design of honeycomb-like A-TNT arrays^[33] helps distribute, rather than localize, the mechanical force at the nanoscale. Based on the structure of the A-TNT arrays, the infiltrated viscoelastic polymer matrix mimics the load-dissipation and lubrication effects of glycosaminoglycans in the natural ligaments,^[19,20] which additionally enhances the energy dissipation of the PIL since molecular chains of the polymer can convert mechanical loading into deformation and heat energy. Additionally, the nanoscale dimensions of A-TNTs and infiltration of the polymer matrix provide extremely abundant interfaces. Therefore, the interfacial sliding between these two components results in a large density of localized high-energy dissipation regions within the structure of the PIL, which can prevent localized nanocracks from coalescing and propagating (Figure 2g).^[34,35] Moreover, due to the highly oriented arrangement of the nanotubes, interface sliding can be significantly improved.^[36] Thus, we were able to demonstrate

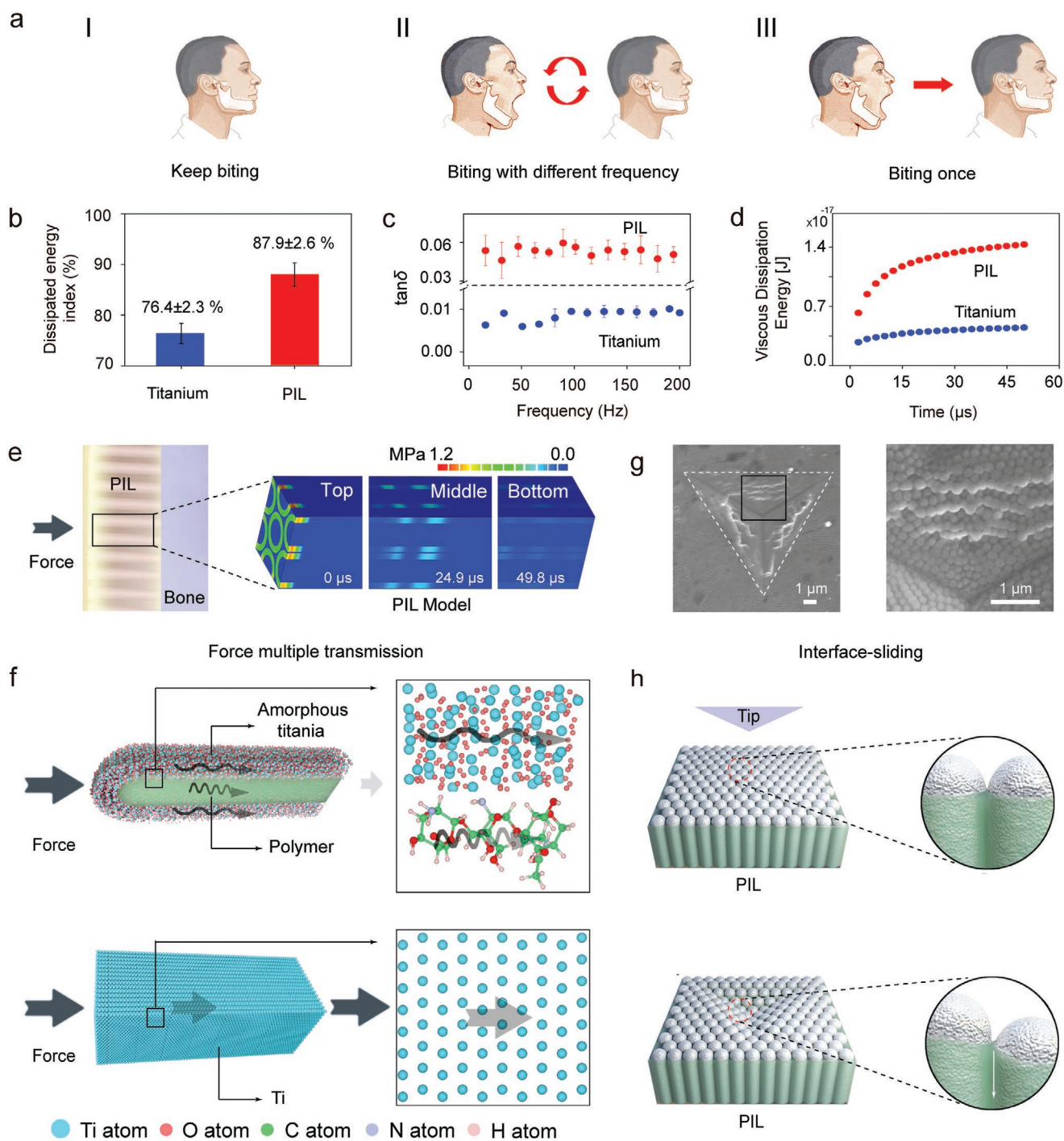


Figure 2. Energy-dissipation properties of the PIL. a) Schematic illustration of the PIL with three typical occlusion situations, including biting into food (I), a continuous chewing motion (II), and instantaneous occlusion (III). b) Energy dissipation index of the titanium and PIL during a contact cycle under static nanoindentation test, and quantified energy dissipation capability. c) NanoDMA (nanoscale dynamic mechanical analysis) nano-indentation tests used to measure the $\tan\delta$ coefficient for titanium and PIL by a frequency sweep with a varied frequency range (ω , from 1–200 Hz). d) Simulation results from finite element modeling (FEM) of the viscous dissipation energy for the titanium and PIL. e) FEM of the PIL after impact loads were applied to the top boundary of the models, and corresponding images of the 3D mechanical contour-mapped regions at different times. f) Cell model of the Ti and PIL corresponding to the dissipative state, after impact loads were applied to the top boundary of the models. g) Top-view low-magnification SEM images of the entire indentation residues, depicting the permanent deformation region. Top-view higher-magnification SEM images of the indentation residues at the sharp indenter regions indicate the occurrence of slippage of the nanotubes. h) Schematic illustration of the nanotube slippage in the PIL during the indentation test.

the function and mechanism of the PIL in optimizing the energy-dissipation of the implant.

To determine whether the PIL is biocompatible for clinical applications, we characterized its influence on cellular vitality and differentiation behavior of bone marrow stem cells of a rat femur (rBMSCs) in vitro. The cellular vitality assay by the cell-counting kit-8 (CCK8) (Figure S16a, Supporting Information) and Cyquant method demonstrated (Figure S16b,c, Supporting Information) that there was no significant difference in proliferation activity of rBMSCs cultured on the Ti substrate, Ti with A-TNTs, and Ti with the PIL. This result indicates that the PIL excludes the adverse effect that might result from the use of glutaraldehyde as a cross-linking agent, thereby providing a biological friendly micro-environment.^[37,38] According to previous studies, we additionally explored the osteogenic differentiation behavior of mesenchymal stem cells (MSCs) on these surfaces in vitro.^[39,40] The gene expression via reverse transcription-polymerase chain reaction (RT-PCR) showed that the osteogenic markers (alkaline phosphatase: ALP; collagen 1 α 1: Col-1; osteopontin: OPN; osteocalcin: OCN; runt-related transcription factor 2: RUNX-2; osteoprotegerin: OPG; and bone morphogenetic protein 2: BMP-2, shown in Table S3, Supporting Information) were 1.5 to three times higher in the PIL group than in the Ti group after 7 days (Figure S16d, Supporting Information) and 14 days (Figure 3a). Furthermore, the quantitative data of *para*-nitrophenol (Figure 3b) demonstrated superior ALP activity and osteogenic differentiation capability of MSCs on the PIL compared with the other two surfaces after 7 and 14 days of culture. These results were corroborated by immunofluorescence staining of osteogenic relative proteins, with more significant RUNX-2, OPN, and OCN production observed on the PIL than in the other groups after 7 and 14 days (Figure 3c and Figure S16e, Supporting Information). Herein, these in vitro results suggest that the PIL possesses superior inductivity by expression of osteogenic specific esterase, genes, and proteins.

To verify whether the PIL could enhance osseointegration in vivo, we performed rat femur implantation surgeries in line with a classical implant surgery model (Figure 3d and Figure S17a, Supporting Information).^[41] New bone formation was characterized using 3D micro-computed tomography (micro-CT), hard-tissue histological sections, and the respective statistical analyses. As shown in Figure 3e top and Figure S17c, Supporting Information, more new bone formed around the PIL implant after 4 and 12 weeks of implantation. Measurements of the ratio of bone volume to total volume in Figure S17d, Supporting Information confirmed that 14% more bone was formed around the implants with the PIL than with Ti. In accordance with the bone volume, the micro-interfaces between new bone and the implants were observed in hard-tissue histological sections stained with methylene blue–acid fuchsin. More typical cortical bone structures appeared in the PIL group after 4 and 12 weeks of implantation (Figure 3e bottom). Quantitative data analyzed from the contact between the bone and implant illustrated an enhanced integration of bone anchorage around the PIL of \approx 18%, compared with bone anchorage to Ti after 12 weeks (Figure 3f). Furthermore, to test the osseointegration shear strength between the bone and different implants, we applied a push-out test after animals were sacrificed after 12 weeks of growth (Figure S17b, Supporting

Information). As shown in Figure 3g, the highest anchorage shear strength was achieved around the implant with the PIL. These results indicate that implants modified with the PIL could dramatically enhance the quality of osseointegration in vivo. Of note here is that the amorphous titania is stable without phase transformation at the physiological conditions of nearly constant body temperature at \approx 37 °C (Figure S18, Supporting Information).

The outstanding osseointegration of the PIL can be ascribed to the synergistic effect of the osteoinductive nanotopography and the cross-linked chitosan component. As noted in previous studies,^[42,43] the topological structure of the nanoscopic A-TNTs, with a diameter of 60 to 80 nm, has been shown to significantly promote osteogenic differentiation of stem cells which simulate the X collagen of the bone matrix. In addition, covalent cross-linked chitosan has been demonstrated to be one of the desirable osteogenic components for guiding bone regeneration due to its superior protein adsorption and hydrophilic surface.^[18,44] The surface of the combination of cross-linked chitosan and A-TNTs in the PIL presents the highest hydrophilic feature characterized by the water contact angle test shown in Figure S19, Supporting Information. With contact to the prevailing nano-topological structure and a superior strong osteogenic component, rBMSCs on the PIL show obvious expression of integrin (Itg) complex, especially integrin β 1 (Figure 3h,i). We further observed the triggered expression of focal adhesion kinase (FAK) within 1–3 days after culturing rBMSCs onto the PIL around the region of the focal adhesion complexes (Figure 3h,i and Figure S17e, Supporting Information). These results indicate that the PIL provides for excellent cell adhesion. Downstream, we demonstrated that genes and proteins involved in the MAPK (mitogen-activated protein kinase) passageway (extracellular signal-regulated kinase (ERK) 1/2, adenosine 5'-monophosphate (AMP)-activated protein kinase (AMPK), and *Drosophila* mothers against decapentaplegic homolog 1 (SMAD1) protein) were upregulated on the PIL implant within 1 day (Figure 3h,j). This is consistent with previous reports that stimulation from FAK could trigger activation of its downstream molecules in the MAPK osteogenic passageway.^[45] Established literature has indicated that the activation of MAPK by the ERK signal could lead the transcriptional activity upregulation of osteogenic biomarkers like OPN, COL-1,^[46] and especially activate SMAD, and induce the phosphorylation of RUNX2 to modulate cell differentiation.^[47] Furthermore, the immunofluorescence and western blot results exhibited nuclear transfer of yes-associated protein (YAP); moreover, significantly high expression of RUNX2 could be detected early on the PIL surface (Figure 3h,k). The biochemical signal from AMPK and the mechano-signal from organized cytoskeletal fibers could also facilitate the nuclear transfer of YAP.^[48,49] Strong evidence indicates that BMSCs are regulated by some biological signals on differentiation into bone tissue via the Hippo-YAP pathway.^[50] The pathway plays a synergetic role in osteogenesis, angiogenesis, and osteoimmunology during the bone formation process around the peri-implant tissue.^[50] Therefore, we propose that the PIL surface could activate apparent mechanosensing of FAK/MAPK and YAP nuclear translocation to significantly enhance osseointegration (Figure 3l).

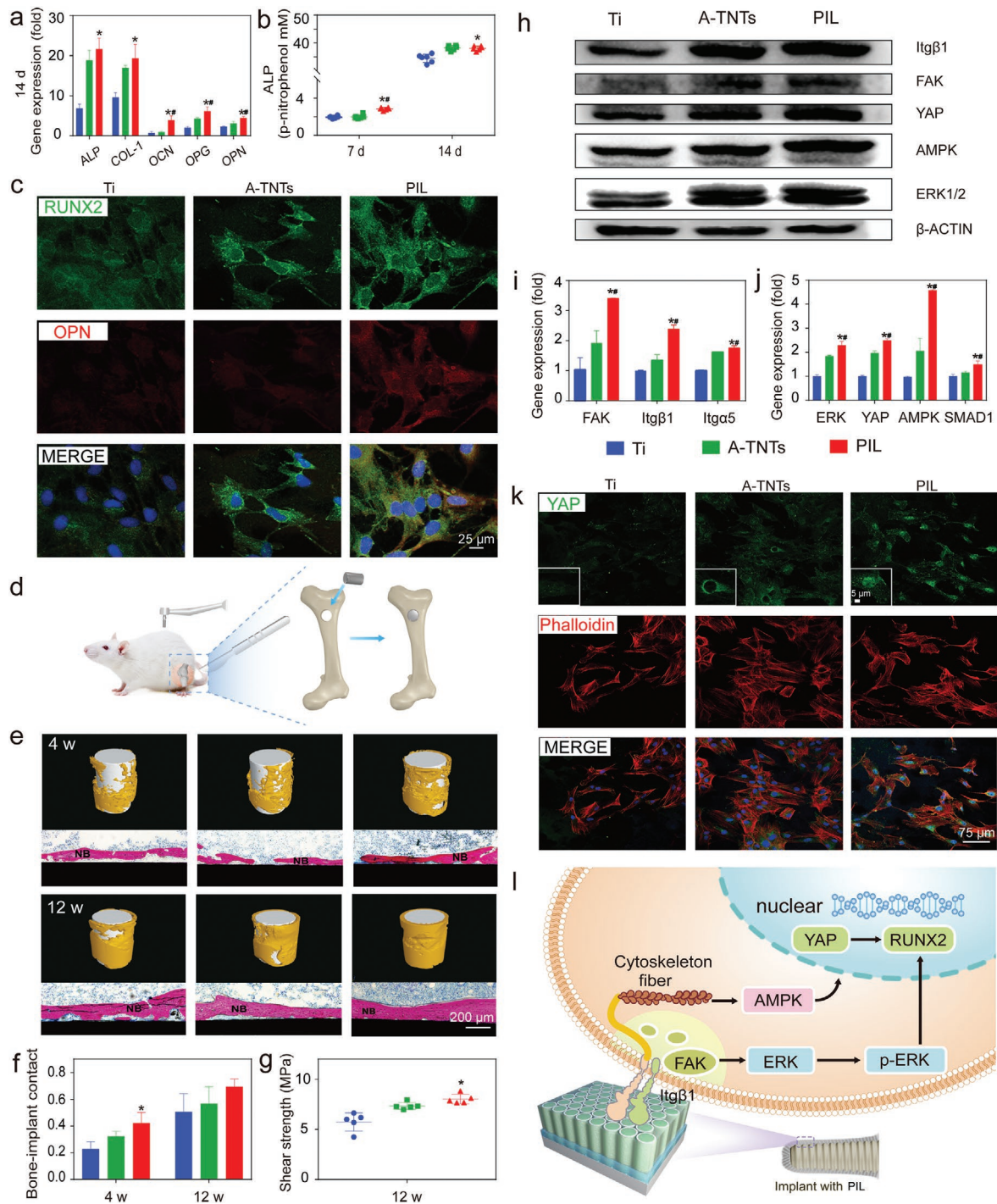


Figure 3. Osteogenic behavior induced by the PIL. a) qRT-PCR showing the high expressions of osteogenic relative genes (ALP/OPN/OPG/OCN/COL-1) on the PIL after osteoinductive culture for 14 days. b) Quantitative results showed that the ALP relative expression of PIL was higher than the titanium and A-TNT groups. c) Immunofluorescence staining shows that both RUNX-2 and OPN clustered on rBMSCs on the PIL surface after osteoinductive culture for 7 days. d) Schematic diagram of the rat femur implant surgery. e) 3D reconstructed images from micro-CT test (above) and histological analysis of bone-implant interfaces. f) Bone-implant contact results collected from histological analysis showed the strongest osteointegration of the PIL after 4 and 12 weeks. g) Push-out test demonstrated the superior shear strength between the bone and implant with the PIL. h) Western blotting analysis after osteoinductive culturing for 3 days indicating upregulated levels of mechanosensing and mechano-transduction proteins (Itgβ1, FAK, ERK, AMPK, and YAP) on the surface of PIL compared with the Ti and A-TNTs foil. i, j) qRT-PCR quantification presents significant higher expression of mechanosensing relative gene (Integrin α5, β1, FAK, ERK, and YAP, SMAD1 and AMPK) in the cells cultured on PIL surface only after 1 day osteoinductive culturing. k) YAP nuclear translocation can be observed apparently on cells of the PIL after osteoinductive culturing for 3 days through immunofluorescence staining. l) A schematic representation of molecular signaling that mediates the osteogenic signal on PIL. The symbol “*” was used for $p < 0.05$ versus corresponding Ti group. While the symbol “#” was introduced for $p < 0.05$ versus corresponding A-TNTs group by one-way ANOVA.

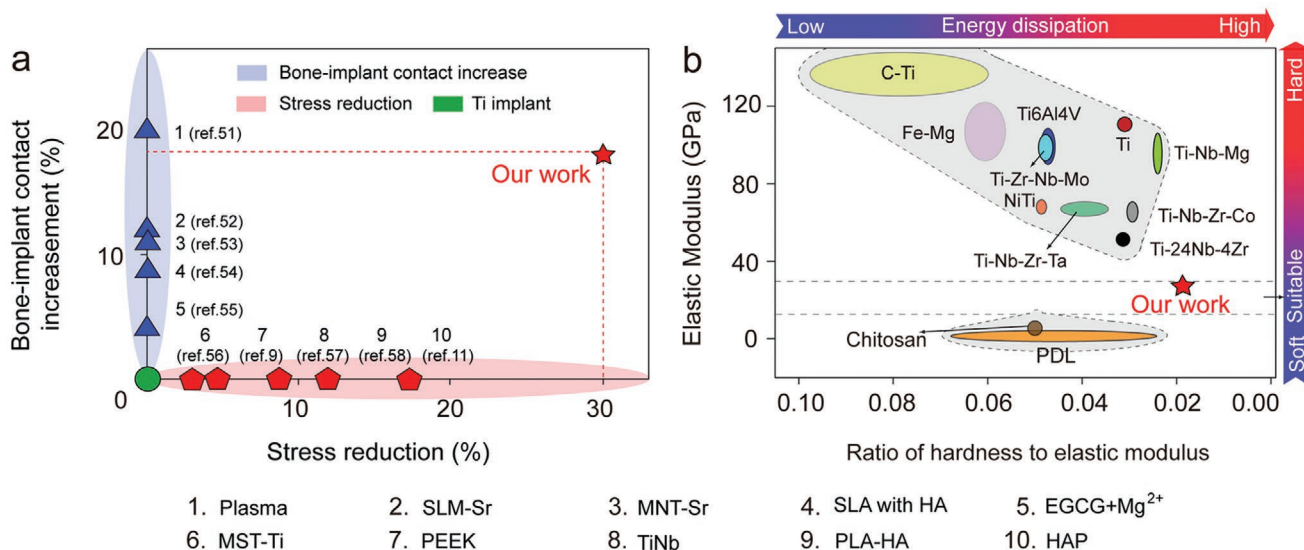


Figure 4. Comparison of the properties of the PIL with other materials.^[9,11,51–58] a) The PIL possesses both stress reduction and increased osteointegration capability compared with the other published materials. Red five-pointed star: values for the PIL; green circle (horizontal and vertical axis): values for the Ti implant, respectively; blue triangle: values for alloys and other coating materials;^[51–55] red pentagon: values for alloys and other coating materials.^[9,11,56–58] b) Elastic modulus vs hardness-to-elastic modulus ratio measured for the PIL, traditional biomedical implant, PDL, and chitosan.

We also compared the value of the stress transfer from implant to peri-implant bone and bone–implant contact of our PIL with other typical or modified Ti implants. The implants contain alloys and other implant coating materials including plasma treatment of titanium (plasma),^[51] Sr-incorporated selective laser melting titanium (SLM-Sr),^[52] Sr-incorporated micro/nano rough titanium (MNT-Sr),^[53] sand-blasting and large-grit acid etching with hydroxyapatite (HAP) nano-coating (SLA with HA),^[54] epigallocatechin gallate and magnesium ions (EGCG+Mg²⁺),^[55] micro-arc oxidation surface-treated titanium (MST-Ti),^[56] polyether ether ketone,^[9] TiNb,^[57] poly(lactic acid) hydroxyapatite (PLA-HA),^[58] and HAP^[11] (Figure 4a). Enhancing osteointegration or energy-dissipation can only be achieved separately in existing implants. However, the PIL simultaneously exhibits a better bone–implant contact and stress reduction transfer from implant to peri-implant bone compared to the other published materials.

Bao and co-workers have proposed a relationship between the ratio of hardness to elastic modulus and energy dissipation based on a depth-sensing indentation technique.^[59] They found that the smaller the ratio of hardness to elastic modulus, the greater the energy dissipation of the material. It is worth noting that the specific values of hardness and elastic modulus for the PIL were clearly the smallest compared to traditional biomedical implants, PDL^[60] and chitosan^[61] (Figure 4b), whereas the stiffness of the PIL is almost the same as that of human bone. However, the energy-dissipative properties of traditional biomedical implants with high elastic moduli are prone to degenerate gradually because of their lower energy dissipation, such as Carbon–Ti,^[62] Fe–Mg,^[63] Ti6Al4V,^[64] NiTi,^[64] titanium, Ti–Zr–Nb–Mo,^[65] Ti–Nb–Mg,^[66] Ti–Nb–Zr–Ta,^[67] Ti–24Nb–4Zr,^[68] and Ti–Nb–Zr–Co.^[68] However, owing to the periodontium-mimetic architecture of the current polymer-infiltrated amorphous titania-nanotube-array, the PIL could simultaneously enhance the osteointegration and energy-dissipation.

3. Conclusion

We have demonstrated the simultaneous enhancement of energy-dissipation and osteointegration to a conventional metal implant. This PIL helps the implant not only achieve load-bearing support but also prevents overload-induced bone resorption. The methodology proposed here could potentially be integrated onto various types of stiff biomaterials, therefore offering promising opportunities toward developing new hard-tissue substitutes with prolonged lifespans and improved functionality. Furthermore, the basic principles of the fabrication and the new functional mechanism of our PIL could have broad technological implications for precise microscale instruments of acoustic absorbers, vibration damping, flexible insulation for aviation, and industrial or military applications.

4. Experimental Section

Growth of the Amorphous Titania Nanotubes Array with a Compact Oxide Layer: In order to match different experimental conditions, suitably shaped titanium substrates were selected. For example, circular titanium (Ti) foils (purity 99.7%), with a diameter of 20 mm and thickness of 0.5 mm, and cylindrical titanium rods, with dimensions of $\Phi 2$ mm (Φ : diameter) \times 4 mm (height) were sequentially cleaned in alcohol, acetone, and deionized water ultrasonically and dried in a vacuum oven at 50 °C for 2 h. The Ti substrates were used as the working electrode with a platinum mesh serving as the counter electrode. The cleaned Ti substrates with different shapes were anodized in 0.57 wt% NH₄F solution in ethylene glycol/hydrogen peroxide (25:1/v: v) at 59 V for 30 min at 20 °C. After removing the resulting amorphous A-TNTs ultrasonically, the circular Ti substrate with a textured surface was anodized again, at 59 V for 2 h at 20 °C, to achieve relatively ordered A-TNTs. The cylindrical Ti rods (purity 99.7%) were again anodized for \approx 3 h; the anodization time was increased due to the limited dimensions of the rod. Subsequently, the differently shaped Ti substrates with the as-formed A-TNTs were transferred into a fluoride-free electrolyte (5 wt% H₃PO₄ solution in ethylene glycol) and an additional anodization

was performed at 59 V for 5 min to fabricate a layer of compact oxide between the A-TNTs and the underlying substrate. The A-TNTs array was finally rinsed separately three times with alcohol, and dried in a vacuum oven at 50 °C for 2 h. The average height of the A-TNTs with a compact layer was measured to be $\approx 8.5 \mu\text{m}$; the titania nanotubes all had a nominally similar inner diameter of $\approx 80 \text{ nm}$.

Fabrication of the PIL: The pale-yellow color of the chitosan solution turned to dark yellow as glutaraldehyde was added and the solution was stirred at 35 °C overnight; this indicated the occurrence of a cross-linking reaction between the cross-linked chitosan (CS) and glutaraldehyde (GA). The final solution had a composition of 0.4% glutaraldehyde, 0.6% chitosan, and 4% acetic acid. Subsequently, the A-TNTs array was immersed in the cross-linked CS solution in vacuo for 2 days to ascertain that all of the space within the nanotube arrays were filled by the solution; this was followed by vacuum drying at room temperature. The PIL was obtained after two deposition procedures; it was then utilized for micromechanical testing and in vitro experiments.

To prepare the samples for in vivo animal experiments, the A-TNTs array on a cylindrical titanium rod substrate was also immersed in cross-linked chitosan solution in vacuo for 2 days, followed by vacuum drying at room temperature. Once more, the PIL was obtained after two deposition procedures.

Fabrication of the Bulk Amorphous and Crystalline Titania: After selecting suitable normal titanium foils (purity 99.7%) with the area of $25 \times 10 \text{ mm}^2$, they were sequentially cleaned in alcohol, acetone, and deionized water ultrasonically and dried in a vacuum oven at 50 °C for 2 h. These Ti foils were used for the working electrode with a platinum mesh serving as the counter electrode. The titanium foils were cleaned and then anodized in 0.57 wt% NH_4F solution in ethylene glycol/hydrogen peroxide (25:1 v/v) at 59 V for 30 min at 20 °C. After removing the ultrasonically cleaned A-TNTs array, the titanium foils with a textured surface were anodized again for 72 h to develop a fairly thick and dense array structure. To obtain crystalline titania with the anatase phase, the amorphous titania was calcined at 673 K for 240 min in a tube furnace.

Sample Characterization: The microstructure of the samples was characterized using SEM (FEI Quanta 250 FEG); the elemental compositions of the PIL were also observed by SEM (7500F, JEOL). To prepare samples for the TEM, the A-TNTs were scraped off the Ti substrate with a knife, ultrasonically dispersed in ethanol, and transferred onto a TEM copper grid. High-resolution TEM (HRTEM) imaging and SAED were used with a Cs-corrected Titan G2 TEM operating at an accelerating voltage of 300 kV. EELS mapping was performed on the 200 kV field-emission STEM (JEOL JEM-ARM200F) equipped with the Gatan Tridiem EELS. X-ray diffraction was carried out using a Shimadzu Lab XRD-6000 instrument with $\text{Cu K}\alpha$ radiation (with a wavelength $\lambda = 0.15406 \text{ nm}$) to characterize the phase structure of A-TNTs. The scan range was $10^\circ\text{--}80^\circ$ (2θ) with the scan rate set as 4° min^{-1} . Thermo gravimetric analysis (TGA) was performed using an apparatus (NETZSCH STA 449F3) with a flowing air with a ramp rate of $10^\circ \text{ C min}^{-1}$ of air from room temperature to 800 °C. Raman spectra analysis was conducted using a high-resolution confocal Raman spectrometer (LabRAM HR-800, Horiba Jobin Yvon). An incident He–Ne laser with an excitation wavelength of 514 nm was used with a $\times 50$ L objective employed to focus the laser beam. The Raman spectra were acquired for 30 s with three accumulations with the laser power set at 1.5 mW and the laser spot area as $1.54 \mu\text{m}^2$ in all acquisitions. Fourier transform infrared spectroscopy (FTIR) measurements were performed using a Thermo Nicolet Nexus-470 FTIR spectrometer at room temperature. The latter measurements were performed on chitosan samples before and after the cross-linking treatment. Samples were put on a silicon wafer and placed in an IR spectrometer with the samples being scanned 64 times with a resolution of 2 cm^{-1} over the scanning range of 700 to 4000 cm^{-1} . The contact angle was measured using an optical contact angle meter system (OCA40Micro, Dataphysics Instruments GmbH, Germany).

Mechanical Testing: All mechanical tests were conducted at room temperature at a relative humidity of $\approx 25\%$. At least five specimens were tested to obtain all the measurements for the static nanoindentation and nanoscale Dynamic Mechanical Analysis (Nano DMA) testing.

Static Nanoindentation: The micromechanical properties of the PIL, titanium, A-TNTs, and the polymers were evaluated by nanoindentation. Static nanoindentation was performed with a TI950 triboindenter (Hysitron, Minneapolis, MN, USA) equipped with a Berkovich diamond tip (radius of curvature $R \approx 100 \text{ nm}$). The Young's modulus and hardness of the samples were measured at a depth of $\approx 10\%$ of the total thickness to avoid substrate and surface effects. For the PIL, the loading sequence consisted of a 35 s loading to 20 mN, followed by a 10 s hold at the same force and then a 10 s unloading. For titanium, the loading sequence consisted of a 55 s loading to 75 mN, followed by a 10 s hold at the same force and then a 15 s unloading. For chitosan and cross-linked chitosan, the loading sequence consisted of a 15 s loading to 10 mN, followed by a 10 s hold at the same force and then a 15 s unloading, respectively. The modulus and hardness were calculated from the unloading curve of each sample by using the Oliver–Pharr method.^[69]

Nano DMA Measurements: A Hysitron TI 950 TriboIndenter was used to characterize the dynamic mechanical properties of PIL and titanium, with a Berkovich tip used for the evaluations. A contact depth, smaller than 10% of the total sample thickness, was employed for the measurements on the PIL and the titanium. For each sample, the storage modulus (E') and loss factor ($\tan\delta$) were determined by a frequency sweep involving a range of frequencies. The frequency of the oscillating load was varied for the frequency sweep test, with an oscillating force superimposed onto a larger open-loop constant quasi-static load. The resulting displacement amplitude and phase shift were used to calculate the values of E' and $\tan\delta$ at each frequency. Several contact depths were selected for each sample. The load functions were specifically varied along the sample and the contact depth for viscoelastic characterization of the PIL.

Finite Element Method (FEM) Simulation of the Bone–Implant Complex: Finite element simulations were performed to evaluate the mechanical functions of the PIL in the bone–implant complex. In this study, the ABAQUS code (SIMULIA) was used to construct mesh models for the alveolar bone and titanium implant. Specifically, the specifications of the implants were as follows: an apex angle of the screw thread, 60° ; thread pitch, 0.6 mm; height of the screw thread, 0.31 mm; diameter, 2 mm; and length, 4 mm.^[70] The thickness of the PIL was set at $9 \mu\text{m}$ which was readily fabricated by the current methods. The dimensions of the alveolar bone were $\Phi 5.4 \text{ mm} \times 6 \text{ mm}$. The material parameters required as inputs for the modeling were set to be consistent with those reported or measured for the titanium implant, alveolar bone, and PIL. Specifically, the elastic moduli were measured to be 113.7 GPa and 27.6 GPa for the titanium implant and the PIL, respectively, as determined by the nanoindentation experiments. An elastic modulus of 24.3 GPa and a Poisson's ratio of 0.3 were chosen for the alveolar bone, consistent with published data.^[71] Subsequently, the implants, with and without the PIL, were inserted into the alveolar bone as simulations which were then carried out under the same loading conditions. The bone and implant were assumed to have a frictional interface with a friction coefficient of 0.3, which allowed for mutual displacement. The occlusal surface of the alveolar bone was subjected to a vertical load of 200 N in normal function representing the process of occlusion. The von Mises stresses caused by the loading forces were analyzed for the peri-implant bone. The resultant stress under such loading conditions was found to be much smaller than the yield strength of the titanium; accordingly, the titanium implant was modeled to be linear elastic. By comparison, the PIL was considered to be nonlinear viscoelastic with a $\tan\delta$ of 0.052. It was noted here that the PIL was set as a homogeneous material without considering its internal nanostructures because of difficulties in modeling. The effects of these nanostructures were further evaluated by finer-scale modeling simulations where only several titanium tubes were involved.

FEM Simulations of the PIL under Impact: The dynamic energy dissipation behavior of the PIL was analyzed by applying an impact load at one end of composite unit and monitoring the propagation of the resulting stress wave with time toward the other end; this was used to simulate the situation of physiological occlusion. The dimensions of a representative 3D unit structure were $0.24 \times 0.24 \times 9 \mu\text{m}^3$, as shown in

Figure S15, Supporting Information and Figure 2e. The unit consisted of one entire titania nanotube filled with cross-linked chitosan at the center combined with six halves at the periphery, that is, containing a total of four nanotubes. Specifically, the outer diameter, wall thickness, and length of the A-TNTs were set by experiment to be 120 nm, 20 nm, and 9 μm , respectively. For comparison, a pure titanium unit with the same dimensions was also analyzed. The elastic moduli of the cross-linked chitosan and titanium were set to be 4.98 and 113.7 GPa, respectively, again consistent with the values measured experimentally by nanoindentation. The elastic modulus for the amorphous titania was taken to be 150 GPa, based on measurements reported in the literature.^[72] In addition, the stress level and time duration were set as 0.1 MPa and 0.1 μs for the impact loading on the unit. A linear elastic model was chosen for the mineral and metal material while a linear viscoelastic model was employed for the polymeric material. It is well known that the propagation time, characteristic length, and the model structure are closely correlated with each other in the dynamic behavior of viscoelastic materials. In the current study, the characteristic length of the unit was set to be consistent with the height of the A-TNTs. The decrease in stress, over the distance from the impact surface, and the viscous dissipation energy were both examined to evaluate the stress wave attenuation over the time for a stress wave to pass through a unit. Under the same impact loading, the viscous dissipation energy was positively correlated with the stress attenuation, as shown in Figure 2d. The simulations and analyses were again performed using the commercial software ABAQUS code (SIMULIA).

Adhesion Strength between the A-TNTs Layer and Titanium Substrate: Samples were first embedded into a self-curing resin with the surface of the testing area exposed. Then, a metal rod was bonded onto the testing area of the A-TNTs layer with epoxy resin (A and B glue). After applying the mixture of A and B glue together, the sample with the testing stretching rod was placed at room temperature for 12 h, whose bonding strength was ≈ 90 MPa, that is, much higher than the adhesion between A-TNTs layer and titanium substrate. A force was then applied to pull the rod away from the sample and the separation interface was exposed between A-TNTs and titanium substrate (Universal Testing Machine, Instron5969, USA). The maximum complete separating force was recorded to calculate the adhesive strength between A-TNTs layer and titanium substrate.

In Vitro Degradation Test: The initial weight (W_{t_0}) of the PIL was measured using an electronic balance. The samples were then incubated in 20 mL of phosphate buffer solution (PBS) (pH 7.4) containing 4 mg mL⁻¹ of lysozyme (Sigma, St. Louis, MO, USA) on a shaker set operating at 40 rpm at a temperature of 37 °C. The solution was changed daily. After soaking for 1, 2, and 3 months, the PIL samples were removed from the degradation medium, washed with distilled water, and dried. The weight (W_{t_d}) of the degraded PIL was then measured, with the percentage weight (W_{t_d}/W_{t_0}) recorded at each time interval.

Cell Culture: Rat bone marrow MSCs (Cyagen Biosciences, Inc. USA) were purchased and cultured with α -MEM medium (Hyclone Laboratories, Inc. UK) supplemented with 10% FBS (foetal bovine serum, Gibco, Thermo Fisher Scientific, USA) at 37 °C in a 5% CO₂ atmosphere. All of the samples, viz. the pure titanium foil, titanium foil with A-TNTs, and titanium foil with the PIL, were sterilized with Cobalt 60 irradiation. Foils were first placed in 12-cell plate (Costar, Corning, USA) and then cells at third to sixth passage were used with an initial seeding density of 1×10^8 cells m⁻². The culture medium was changed every 2 days. For evaluation, the basic osteogenic differentiation medium (Cyagen) was further used to culture the rBMSCs in differentiation assays.

Cell Proliferation and Viability: Cell counting-8 (CCK-8, Dojindo Laboratories, Japan) and to CyQuant cell proliferation assays (Cell proliferation assay kit, C35006 Thermo Fisher) were performed to evaluate the cell proliferation and viability. For CCK-8, after cells were cultured on different foils for 1, 3, 5, and 7 days, CCK-8 reagent was added into the plate and incubated for 2 h. The relative cell number was determined by measuring the light absorbance (OD) at a wavelength of 450 nm of the formazan dye generated in the cultures. For the Cyquant test, the foils with cells were gathered at 1, 4, and 7 days and dyed with

the testing kit after rinsing with PBS. The results were observed with fluorescence microscopy. The images were gathered randomly and the cells were counted using Image Pro Plus 6 software.

ALP Viability: The rBMSCs were cultured onto different foils for 7 and 14 days with an osteogenic differentiation medium and lysed by lytic fluid (Beyotime P0013), China) with centrifugation at 12 000 rpm for 5 min. The supernatant was collected for the detection of ALP activity (Beyotime P0321S). The final absorbance to ALP was detected using a spectrophotometric microplate reader 490 nm.

Expression of Genes Level through Real-Time Quantitative-PCR (qRT-PCR): Cells were cultured on different titanium substrates for 1, 3, 7, and 14 days. The total RNA was extracted and reversely transcribed for cDNA with RNA extract and PrimeScript RT reagent kit (Takara Co. Japan), respectively. Only the extracted RNA met the standard of OD:260/280 = 1.8–2.0 during the concentration test could be further used. The obtained cDNA was further amplified via a real-time quantitative-PCR (qRT-PCR) technique under the following amplification conditions: 95 °C for 30 s, following by 39 cycles of 95 °C for 5 s and 60 °C for 30 s. All primer sequences for target genes (OPN, OCN, COL-1, BMP2, RUNX2, OPG, ITG $\alpha 5$, ITG $\beta 1$, FAK, ERK1/2, YAP, SAMD1 AMPK, and GAPDH) are presented in Table S3, Supporting Information.

Immunofluorescence Analysis: The samples cultured with cells were rinsed three times with PBS and fixed in 4% paraformaldehyde for 15 min at room temperature. The samples were then permeabilized with 0.1% Triton X-100 (diluted with PBS) for 10 min and blocked with 3% bovine serum albumin (BSA; diluted with PBS) for 1 h at room temperature. The permeabilization solution was removed, and the samples were rinsed with PBS for 5 min at room temperature. The 3% BSA was used to reduce nonspecific staining. The samples were incubated with the following primary antibodies in 5 wt% BSA in PBS overnight at 4 °C: polyclonal rabbit anti-RUNX2 (1:100; Abcam, ab264077, USA), polyclonal rabbit anti-OPN (1:200; Abcam, ab63856), monoclonal rabbit anti-OCN (1:250; Abcam, ab93876), polyclonal rabbit anti-YAP1 (1:1000; Abcam, ab62751), and polyclonal rabbit FAK (1:200; Abcam, ab40794). After thorough rinsing was performed to remove excess antibodies, the cells were incubated with the following secondary antibodies for 1 h in the dark: donkey anti-rabbit IgG H&L Alexa Fluor 594 (1:500; Abcam, ab150076) and preadsorbed goat anti-rabbit IgG H&L Alexa Fluor 488 (1:500; Abcam, ab150081). Phalloidin (Sigma) was used for cytoskeletal staining with 4',6-diamidino-2-phenylindole (DAPI; Sigma) used to stain the nuclei. Images were acquired using a confocal laser scanning microscope (Leica, USA).

Western Blot Analysis: Cells on different substrates were lysed in radioimmunoprecipitation assay (RIPA) buffer (Beyotime) containing a protease and phosphatase inhibitor cocktail (Thermo Fisher Scientific) and were then centrifuged at 12 000 rpm for 20 min at 4 °C. The supernatants were gathered after centrifugation. A bicinchoninic acid (BCA) protein assay kit (Beyotime) was used to determine the protein concentration. The samples were then mixed with 6 \times SDS loading buffer (Beyotime) at a 1:5 ratio and heated for 5 min at 100 °C for protein degradation. 30 μg protein was separated by sodium dodecyl sulfate polyacrylamide gel electrophoresis (SDS-PAGE) and transferred to a poly(vinylidene fluoride) (PVDF) membrane. The membrane was blocked with 5% skim milk (diluted with TBST) for 1 h at room temperature, incubated with primary antibodies overnight at 4 °C (polyclonal rabbit anti-ERK1/2 (1:200; Abcam, ab214362), monoclonal rabbit anti-Itg $\beta 1$ (1:200; Abcam, ab179471), polyclonal rabbit anti-YAP1 (1:1000; Abcam, ab62751), and polyclonal rabbit FAK (1:200; Abcam, ab40794), polyclonal rabbit AMPK (1:200; Abcam, ab32047)), and then incubated with HRP (horseradish peroxidase) conjugated secondary antibodies (Cell Signal Technology, USA). Autoradiograms were obtained using an ECL western blotting substrate. β -actin was used as the internal control.

Animal Experiments: All animal experiments were conducted with the approval of Peking University Biomedical Ethics Committee Office (approval number: LA2019321). Forty 10-week-old male Sprague–Dawley rats were used in this study. The implants in this experiment ($\Phi 2$ mm \times 4 mm) were also sterilized with Cobalt 60 irradiation. The rats were randomly assigned to three groups—A: Ti+ A-TNTs implants;

B: A-TNTs + PIL implants; and C: PIL + Ti implants. The rats were first anesthetized by intraperitoneal injection of 50 mg kg⁻¹ pentobarbital sodium solution. After the distal femur was exposed by skin incision and blunt dissection, teeth plant equipment was used to machine a hole of $\Phi 2$ mm \times 4 mm at the cortical bone in each distal femur, with tooth implant equipment under cooling with saline water. The appropriate distance between the hole and the distal femur growth plate was ≈ 2 to 3 mm. After removing the bone chippings, a sample implant was inserted into the matched hole in each distal femur. The muscular fascia, subcutaneous tissue, and skin were then sutured in sequence. The thermal support was not withdrawn until the rats recovered from the anesthesia. The rats were sacrificed 4 and 12 weeks post-implantation. The femurs were then detached and fixed in 10% neutral buffered formalin 1 day for use in subsequent experiments.

Micro-CT Test: In total, 12 samples of each group were scanned at 4- or 12-week time intervals using a computed micro-tomography X-ray (micro-CT) 3D imaging system (Y. Cheetah, YXLON International GmbH, Germany) at 90 kV, 45 mA, and 1000 ms integration time. The 3D images were reconstructed with an isotropic voxel size of 7 μ m to measure new bone formation on the interfaces at a range of 0.5 mm. BV/TV (bone volume/total volume) values were calculated based on a micro-CT examination of every sample. After 3D visualization, the regions of interest were marked with pseudo colors.

Histological Analysis: Tissue processing and sectioning were carried out as previously described.^[73] After the micro-CT test was finished, 7 samples from every group were used for a sampling site. Briefly, after dehydrating in a series of graded ethanol (70–100%), undecalcified tissue samples were infiltrated in methyl methacrylate resin (Technovit 7200, VLC, Hereaeus Kulzer, Wehrheim, Germany) for 4 weeks and then embedded and polymerized under UV light for 10 h. The samples were then sectioned along the longitudinal axis of the implants with an Exakt saw (Exakt Apparatebau, Norderted, Germany) and were finally ground down to ≈ 25 μ m thickness. Methylene blue–acid fuchsin staining was performed separately on the tissue sections; the calcified bone in the slides was distinguished from the implants and other tissues by its characteristic bright pink color. Histological images were taken under a light microscope (CX21, Olympus, Japan) and were analyzed using the Bioquant Osteo software V7.10.10 (Nashville, TN, USA). Bone–implant contact values (BIC) were performed along the long axis of implant randomly.

Push Out Test: 10 samples from every group were used for this test after completion of the micro-CT scanning. The femur was dissected from the body and both ends of the implant were exposed using a dental clinical diamond bur. The femur was then placed on the sample stage of a mechanical testing machine (Instron 5969 Universal Testing Machine, Norwood, MA, USA). A displacement rate of 1 mm min⁻¹ was set for the test. The maximum force was recorded and the interfacial shear strength was calculated by dividing the force (N) at the point of failure by the surface area of the implant in contact with bone (mm²).

Statistical Methods: Statistical analysis was performed with SPSS v.22.0 software (IBM, Armonk, NY, USA). Differences between groups were evaluated by one-way analysis of variance (ANOVA) with the LSD t-test. A $p < 0.05$ was considered statistically significant.

Supporting Information

Supporting Information is available from the Wiley Online Library or from the author.

Acknowledgements

J.H., Z.X., Z.L., and H.Z. contributed equally to this work. This work was supported by the National Key R&D Program of China (2020YFA0710401, 2020YFA0710403, 2020YFA0710404, 2018YFC1105301, 2018YFC1105302, 2018YFC1105304), the National Natural Science Foundation of

China (51532001, 51772011, 51802010, 52073008, 81922019, 51772006, 31670993), the National Youth Topnotch Talent Support Program (QNB2019-3), Beijing Municipal Science & Technology Commission Projects (Z181100002018001), and the Peking University Medicine Fund (PKU2020LCXQ009).

Conflict of Interest

The authors declare no conflict of interest.

Data Availability Statement

Research data are not shared.

Keywords

amorphous titania nanotubes, energy dissipation, osteointegration, tooth periodontal ligament

Received: May 17, 2021

Revised: July 18, 2021

Published online:

- [1] H. D. Jung, T. S. Jang, L. Wang, H. E. Kim, Y. H. Koh, J. Song, *Biomaterials* **2015**, *37*, 49.
- [2] R. Branemark, L. O. Ohnrell, P. Nilsson, P. Thomsen, *Biomaterials* **1997**, *18*, 969.
- [3] M. Esposito, J. M. Hirsch, U. Lekholm, P. Thomsen, *Eur. J. Oral Sci.* **1998**, *106*, 527.
- [4] S. L. Oh, H. J. Shiau, M. A. Reynolds, *J. Prosthet. Dent.* **2020**, *123*, 54.
- [5] K. Morinaga, H. Sasaki, S. Park, A. Hokugo, H. Okawa, Y. Tahara, C. S. Colwell, I. Nishimura, *Biomaterials* **2019**, *192*, 62.
- [6] X.-Y. Ma, Y.-F. Feng, Z.-S. Ma, X. Li, J. Wang, L. Wang, W. Lei, *Biomaterials* **2014**, *35*, 7259.
- [7] J. Park, S. Bauer, P. Schmuki, K. von der Mark, *Nano Lett.* **2009**, *9*, 3157.
- [8] Y. Hou, W. Xie, L. Yu, L. C. Camacho, C. Nie, M. Zhang, R. Haag, Q. Wei, *Small* **2020**, *16*, 1905422.
- [9] J. Anguiano-Sanchez, O. Martinez-Romero, H. R. Siller, J. A. Diaz-Elizondo, E. Flores-Villalba, C. A. Rodriguez, *Comput. Math. Methods Med.* **2016**, *2016*, 6183679.
- [10] A. L. Sie Kiong, R. Arjunkumar, *J. Pharm. Sci. Res.* **2014**, *6*, 158.
- [11] H. S. Hedia, *J. Med. Eng. Technol.* **2007**, *31*, 280.
- [12] I. A. V. P. Poiate, A. B. de Vasconcellos, R. B. de Santana, E. Poiate, *J. Periodontol.* **2009**, *80*, 1859.
- [13] E. Szymanska, K. Winnicka, *Mar. Drugs* **2015**, *13*, 1819.
- [14] I. Z. Oskui, A. Hashemi, *J. Biomech.* **2016**, *49*, 756.
- [15] T. Nojiri, C.-Y. Chen, D. M. Kim, J. Da Silva, C. Lee, M. Maeno, A. A. McClelland, B. Tse, S. Ishikawa-Nagai, W. Hatakeyama, H. Kondo, M. Nagai, *J. Nanobiotechnol.* **2019**, *17*, 34.
- [16] P. Roy, S. Berger, P. Schmuki, *Angew. Chem., Int. Ed.* **2011**, *50*, 2904.
- [17] D. Yu, X. Zhu, Z. Xu, X. Zhong, Q. Gui, Y. Song, S. Zhang, X. Chen, D. Li, *ACS Appl. Mater. Interfaces* **2014**, *6*, 8001.
- [18] S. Ma, Z. Chen, F. Qiao, Y. Sun, X. Yang, X. Deng, L. Cen, Q. Cai, M. Wu, X. Zhang, P. Gao, *J. Dent.* **2014**, *42*, 1603.
- [19] G. R. S. Naveh, J. E. Foster, T. M. S. Santisteban, X. Yang, B. R. Olsen, *Proc. Natl. Acad. Sci. USA* **2018**, *115*, 9008.
- [20] T. J. Lujan, C. J. Underwood, N. T. Jacobs, J. A. Weiss, *J. Appl. Physiol.* **2009**, *106*, 423.

- [21] S. Ma, M. Scaraggi, D. Wang, X. Wang, Y. Liang, W. Liu, D. Dini, F. Zhou, *Adv. Funct. Mater.* **2015**, *25*, 7366.
- [22] Y. Wang, M. Ludwigson, R. S. Lakes, *Mater. Sci. Eng., A* **2004**, *370*, 41.
- [23] R. S. Lakes, T. Lee, A. Bersie, Y. Wang, *Nature* **2001**, *410*, 565.
- [24] B. Yeom, T. Sain, N. Lacevic, D. Bukharina, S.-H. Cha, A. M. Waas, E. M. Arruda, N. A. Kotov, *Nature* **2017**, *543*, 95.
- [25] E. Buck, H. Li, M. Cerruti, *Macromol. Biosci.* **2019**, *20*, 1900271.
- [26] S. Amini, M. Tadayon, S. Idapalapati, A. Miserez, *Nat. Mater.* **2015**, *14*, 943.
- [27] R. S. Lakes, *J. Compos. Mater.* **2016**, *36*, 287.
- [28] B. Wu, S. Zhao, H. Shi, R. Lu, B. Yan, S. Ma, B. Market, *Angle Orthodontist* **2019**, *89*, 480.
- [29] A. Amato, S. Terreni, M. Granata, C. Michel, B. Sassolas, L. Pinard, M. Canepa, G. Cagnoli, *Sci. Rep.* **2020**, *10*, 1670.
- [30] Y. Si, X. Wang, L. Dou, J. Yu, B. Ding, *Sci. Adv.* **2018**, *4*, eaas8925.
- [31] F. Li, H. Zhao, Y. Yue, Z. Yang, Y. Zhang, L. Guo, *ACS Nano* **2019**, *13*, 4191.
- [32] Y. Wei, S. Liu, Z. Xiao, H. Zhao, J. Luo, X. Deng, L. Guo, *Adv. Mater.* **2020**, *32*, 1907067.
- [33] S. Kumar, J. Ubaid, R. Abishera, A. Schiffer, V. S. Deshpande, *ACS Appl. Mater. Interfaces* **2019**, *11*, 42549.
- [34] L. Ci, J. Suhr, V. Pushparaj, X. Zhang, P. M. Ajayan, *Nano Lett.* **2008**, *8*, 2762.
- [35] C. Xiao, M. Li, B. Wang, M.-F. Liu, C. Shao, H. Pan, Y. Lu, B.-B. Xu, S. Li, D. Zhan, Y. Jiang, R. Tang, X. Liu, H. Colfen, *Nat. Commun.* **2017**, *8*, 1398.
- [36] J. Meaud, T. Sain, B. Yeom, S. J. Park, A. B. Shoultz, G. Hulbert, Z.-D. Ma, N. A. Kotov, A. J. Hart, E. M. Arruda, A. M. Waas, *ACS Nano* **2014**, *8*, 3468.
- [37] L. Lv, Y. Liu, P. Zhang, X. Zhang, J. Liu, T. Chen, P. Su, H. Li, Y. Zhou, *Biomaterials* **2015**, *39*, 193.
- [38] C. D. Ji, A. Khademhosseini, F. Dehghani, *Biomaterials* **2011**, *32*, 9719.
- [39] Y. Zhang, J. Xu, Y. Ruan, M. Yu, M. O'Laughlin, H. Wise, D. Chen, L. Tian, D. Shi, J. Wang, S. Chen, J. Feng, D. Chow, X. Xie, L. Zheng, L. Huang, S. Huang, K. Leung, N. Lu, L. Zhao, H. Li, D. Zhao, X. Guo, K. Chan, F. Witte, H. Chan, Y. Zheng, L. Qin, *Nat. Med.* **2016**, *22*, 1160.
- [40] W. Shen, Y. Lai, L. Li, K. Liao, H. Lai, S. Kao, J. Wang, C. Chuong, S. Hung, *Nat. Commun.* **2019**, *10*, 2226.
- [41] Y. Liu, X. Zhang, C. Cao, Y. Zhang, J. Wei, Y. Li, W. Liang, Z. Hu, J. Zhang, Y. Wei, X. Deng, *Adv. Funct. Mater.* **2017**, *27*, 1703771.
- [42] Y. Yu, X. Shen, Z. Luo, Y. Hu, M. Li, P. Ma, Q. Ran, L. Dai, Y. He, K. Cai, *Biomaterials* **2018**, *167*, 44.
- [43] M. J. Dalby, N. Gadegaard, R. O. C. Oreffo, *Nat. Mater.* **2014**, *13*, 558.
- [44] P. Ghosh, A. Rameshbabu, D. Das, N. Francis, H. Pawar, B. Subramanian, S. Pal, S. Dhara, *Colloids Surf., B* **2015**, *125*, 160.
- [45] Y. Wei, S. Jiang, M. Si, X. Zhang, J. Liu, Z. Wang, C. Cen, J. Huang, H. Huang, L. Chen, S. Wang, C. Feng, X. Deng, L. Jiang, *Adv. Mater.* **2019**, *31*, 1900582.
- [46] W. Zeng, Y. Yan, F. Zhang, C. Zhang, W. Liang, *Protein Cell* **2013**, *4*, 539.
- [47] C. Ren, W. Gong, F. Li, M. Xie, *Chin. J. Nat. Med.* **2019**, *17*, 756.
- [48] Z. Meng, Y. Qiu, K. Lin, A. Kumar, J. K. Placone, C. Fang, K.-C. Wang, S. Lu, M. Pan, A. W. Hong, T. Moroishi, M. Luo, S. W. Plouffe, Y. Diao, Z. Ye, H. W. Park, X. Wang, F.-X. Yu, S. Chien, C.-Y. Wang, B. Ren, A. J. Engler, K.-L. Guan, *Nature* **2018**, *560*, 655.
- [49] J. S. Mo, Z. Meng, Y. C. Kim, H. W. Park, C. G. Hansen, S. Kim, D.-S. Lim, K.-L. Guan, *Nat. Cell Biol.* **2015**, *17*, 500.
- [50] A. Zhou, H. Yu, J. Liu, J. Zheng, Y. Jia, B. Wu, L. Xiang, *Front. Cell Dev. Biol.* **2020**, *8*, 780.
- [51] Z. Zheng, X. Ao, P. Xie, J. Wu, Y. Dong, D. Yu, J. Wang, Z. Zhu, H. H. K. Xu, W. C. Chen, *Sci. Rep.* **2020**, *10*, 10637.
- [52] Y. Shimizu, S. Fujibayashi, S. Yamaguchi, S. Mori, H. Kitagaki, T. Shimizu, Y. Okuzu, K. Masamoto, K. Goto, B. Otsuki, T. Kawai, K. Morizane, T. Kawata, S. Matsuda, *Mater. Sci. Eng., C* **2020**, *109*, 110519.
- [53] C. Zhou, A.-T. Xu, D.-D. Wang, G.-F. Lin, T. Liu, F.-M. He, *Biomater. Sci.* **2018**, *6*, 1946.
- [54] J. Lee, J. M. Yoo, H. Ben Amara, Y.-M. Lee, Y.-J. Lim, H. Kim, K.-T. Koo, *J. Periodontal Implant Sci.* **2019**, *49*, 25.
- [55] S. Lee, Y.-Y. Chang, J. Lee, S. K. M. Perikamana, E. M. Kim, Y.-H. Jung, J.-H. Yun, H. Shin, *Biomater. Sci.* **2020**, *8*, 3404.
- [56] P.-J. Hou, K.-L. Ou, C.-C. Wang, C.-F. Huang, M. Ruslin, E. Sugiatno, T.-S. Yang, H.-H. Chou, *J. Mech. Behav. Biomed. Mater.* **2018**, *79*, 173.
- [57] B. Piotrowski, A. A. Baptista, E. Patoor, P. Bravetti, A. Eberhardt, P. Laheurte, *Mater. Sci. Eng., C* **2014**, *38*, 151.
- [58] N. Fouda, B. Eltlhawy, T. El-Midany, *Int. J. Mech. Mechatron. Eng.* **2015**, *15*, 76.
- [59] Y. Bao, W. Wang, Y. Zhou, *Acta Mater.* **2004**, *52*, 5397.
- [60] H. Huang, W. Tang, Y. Yang, B. Wu, B. Yan, *J. Mech. Med. Biol.* **2016**, *16*, 1650089.
- [61] A. Gomez Sanchez, E. Prokhorov, G. Luna-Barcenas, A. G. Mora-Garcia, Y. Kovalenko, E. M. Rivera-Munoz, M. G. Raucchi, G. Buonocore, *Mater. Chem. Phys.* **2018**, *217*, 151.
- [62] M. Zhang, T. Xie, X. Qian, Y. Zhu, X. Liu, *ACS Omega* **2020**, *5*, 22772.
- [63] M. M. Khan, K. M. Deen, I. Shabib, E. Asselin, W. Haider, *Acta Biomater.* **2020**, *113*, 660.
- [64] F. Bartolomeu, M. M. Costa, N. Alves, G. Miranda, F. S. Silva, *Opt. Laser Eng.* **2020**, *134*, 106208.
- [65] P. Chui, R. Jing, F. Zhang, J. Li, T. Feng, *J. Alloy Compd.* **2020**, *842*, 155693.
- [66] E. D. Gonzalez, N. K. Fukumasu, A. L. Gobbi, C. R. M. Afonso, P. A. P. Nascente, *Surf. Coat. Technol.* **2020**, *400*, 126070.
- [67] T. Maity, Ö. Balci, C. Gammer, E. Ivanov, J. Eckert, K. G. Prashanth, *J. Mech. Behav. Biomed. Mater.* **2020**, *108*, 103839.
- [68] J. Zhao, F. Ma, P. Liu, X. Liu, W. Li, D. He, *J. Mater. Eng. Perform.* **2020**, *29*, 3736.
- [69] G. M. Pharr, A. Bolshakov, *J. Mater. Res.* **2002**, *17*, 2660.
- [70] Y.-T. Sul, J. Jonsson, G.-S. Yoon, C. Johansson, *Clin. Oral Implants Res.* **2010**, *20*, 1146.
- [71] X. Liu, K. Lin, C. Wu, Y. Wang, Z. Zou, J. Chang, *Small* **2014**, *10*, 152.
- [72] T. Nakamura, T. Ichitsubo, E. Matsubara, A. Muramatsu, N. Sato, H. Takahashi, *Acta Mater.* **2005**, *53*, 323.
- [73] X. Dai, X. Zhang, M. Xu, Y. Huang, B. Heng, X. Mo, Y. Liu, D. Wei, Y. Zhou, Y. Wei, X. Deng, X. Deng, *RSC Adv.* **2016**, *6*, 43685.